Journal of Materials Chemistry C

ROYAL SOCIETY OF CHEMISTRY

PAPER

View Article Online
View Journal | View Issue

Cite this: J. Mater. Chem. C, 2025, 13, 19699

Moderate-temperature solution-processed synthesis of incommensurate $Sr_{8/7}TiS_3$ thin films and rod-shaped nanocrystals

Kiruba Catherine Vincent, †[a] Shubhanshu Agarwal, †[a] Sofia Rodriguez Perilla, [b] Daniel C Hayes, [a] Kim Kisslinger[c] and Rakesh Agrawal *[a]

Received 30th June 2025,
Accepted 25th August 2025

DOI: 10.1039/d5tc02508g

rsc.li/materials-c

The chalcogenide perovskite family has been steadily gaining increasing attention from the research community due to its optoelectronic properties and potential for diverse applications. While $BaZrS_3$ and $BaTiS_3$ have been the most extensively studied, other promising compounds in this family, such as Sr_xTiS_3 ($1.05 < x < 1.22$), are now being explored for various optical, optoelectronic, and energy storage applications. However, challenges remain in achieving the low-temperature synthesis of Sr_xTiS_3. In this study, we report, for the first time, the synthesis of Sr_xTiS_3 nanocrystals at temperatures below 400 °C. The synthesized nanocrystals exhibit a rod-like morphology. Additionally, we have developed solution-processing routes to synthesize phase-pure Sr_xTiS_3 thin films, marking the first reported instance of such films, at temperatures below 600 °C. We also demonstrate the solid-state synthesis of Sr_xTiS_3 powder below 600 °C. Our work paves the way for new and exciting application avenues for Sr_xTiS_3.

Introduction

Chalcogenide perovskites are an emerging class of earth-abundant inorganic semiconductors, recognized as non-toxic and stable alternatives to lead halide perovskites. These materials crystallize in an ABX_3 structure, where typically the A-site is occupied by Ba, Sr, or Ca; the B-site is occupied by Zr, Hf, or Ti; and the X-site is occupied by sulfur. While Zr- and Hf-based ABX_3 compounds adopt an orthorhombic distorted perovskite structure with corner-sharing octahedra, Ti-based compounds, especially those with Ba or Sr at the A-site thermodynamically favor a hexagonal $BaNiO_3$-type structure characterized by face-sharing octahedra, resulting in rod-like structures. This structural diversity highlights the versatility of this class of materials and their potential for tailored applications in optoelectronics and energy-related fields.[1–3]

$BaZrS_3$ has been widely studied for optoelectronic applications, including photovoltaics and photodetectors. It has been synthesized using both vacuum- and solution-based techniques, with some methods achieving synthesis temperatures below 400 °C.[4–7] Similarly, $BaTiS_3$ has been extensively investigated for thermoelectric applications and has demonstrated significant potential. Additionally, $BaTiS_3$ exhibits high birefringence, making it a promising candidate for various optical applications.[8–12] Notably, it has been synthesized using a variety of techniques, achieving the lowest synthesis temperatures among all the ABS_3 compounds.[6,8,10,13,14] These advancements highlight the versatility and growing interest in these materials for a range of technological applications.

$SrTiS_3$, however, has been studied sparingly and has only been synthesized in powder form, with only one reported attempt to produce thin films. In nearly all cases, it has been synthesized in an incommensurate structure with the formula Sr_xTiS_3, where x ranges from 1.05 to 1.22. However, the composition $Sr_{8/7}TiS_3$ is the most frequently reported in the literature.[15–21] Traditionally, Sr_xTiS_3 has been synthesized by sulfurizing oxide powders using CS_2 at temperatures exceeding 800 °C.[15–21] Similar to $BaZrS_3$ and $BaTiS_3$, Sr_xTiS_3 also demonstrates tremendous potential, exhibiting the highest birefringence among all known inorganic materials.[2,22] Recently, it has been explored as a cathode material in Li–S batteries, showing promising results, and has been briefly investigated for thermoelectric, thermistor and photo-thermoelectric applications.[21,23] These findings underscore its untapped potential for a variety of advanced technological uses.

Given its promise, there is a need to develop methods to synthesize Sr_xTiS_3, particularly at lower temperatures, to reduce

[a] Davidson School of Chemical Engineering, Purdue University, West Lafayette, IN 47907, USA. E-mail: agrawalr@purdue.edu
[b] Chemical and Environmental Engineering, Universidad Nacional de Colombia, Bogota D.C., Colombia
[c] Center for Functional Nanomaterials, Brookhaven National Laboratory, Upton, NY 11973, USA
† Equal contribution.

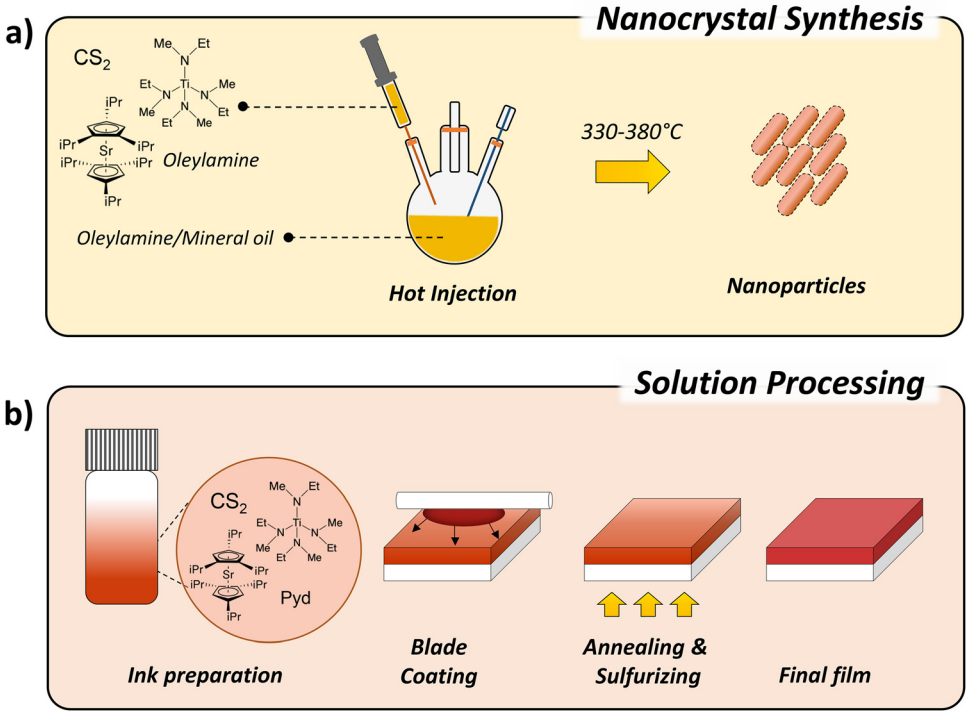

Fig. 1 Schematic illustrating the procedures adopted in this work for synthesizing $Sr_{8/7}TiS_3$ (a) nanocrystals and (b) thin films.

the thermal budget. A possible reason for the high-temperature synthesis could be the use of highly stable metal precursors,[17,19] the absence of a transport agent, and the high oxophilicity of titanium.[24] To address these challenges, this study explores the use of different metal precursors (both reactive and stable) for the solution synthesis of $Sr_{8/7}TiS_3$ nanocrystals and solution-processed thin films (see Fig. 1). Additionally, we utilize our previously reported HfS_3–H_2S shuttle[25] to mitigate oxophilicity concerns during film synthesis. Structural and compositional characterizations have been conducted on the synthesized thin films and nanocrystals. Through this study, we aim to overcome the synthesis challenges associated with $Sr_{8/7}TiS_3$ and unlock its full potential for advanced applications.

Results and discussion

Synthesis of $Sr_{8/7}TiS_3$ nanocrystals

Although $SrTiS_3$ nanocrystals have not been synthesized previously, our group, along with others, has successfully synthesized $BaZrS_3$, $BaHfS_3$, $BaTiS_3$, α-$SrZrS_3$, and α-$SrHfS_3$ nanoparticles.[6,13,26,27] Most of these nanoparticles were synthesized using a ''heat-up'' method, in which organometallic or metal–organic precursors, a sulfur source (primarily CS_2 or a variant of thiourea), and oleylamine as the reaction solvent were heated together to a desired reaction temperature. However, for $BaZrS_3$, a hot-injection approach proved more successful, resulting in a phase-pure synthesis of the orthorhombic *Pnma* phase. In this method, reactive metal precursors were combined with CS_2 to form barium dithiocarboxylate and zirconium dithiocarbamate species. These species, along with excess CS_2 and oleylamine, formed a slurry that was hot-injected into heated mineral oil at temperatures exceeding 360 °C to nucleate phase-pure $BaZrS_3$ nanoparticles. This approach marked the first report of reproducible synthesis of phase-pure orthorhombic $BaZrS_3$ nanoparticles in the chalcogenide perovskite literature.[6]

As previously mentioned, $SrTiS_3$ has been recognized for its impressive array of electronic properties, but its synthesis has remained cumbersome and requires high temperatures. Therefore, developing approaches to synthesize this material at lower temperatures would be a significant advancement. In our previous work, we attempted the heat-up method using similar precursors to synthesize $SrTiS_3$ nanocrystals, but the attempt was unsuccessful and resulted in the formation of binary sulfides.[6] This highlights the need for alternative strategies to overcome the synthesis challenges associated with $SrTiS_3$.

In this report, we employed a slightly modified hot-injection technique, where metal precursors, oleylamine (OLA), and CS_2 were injected into hot mineral oil (375–380 °C). Table 1 provides a list of the acronyms used for the commonly employed chemicals in this study. Unlike in our previous study, we first dissolved $Sr(iPr_3Cp)_2$ and TEMAT in OLA. All dissolution and

Table 1 List of common chemicals and their acronyms used in this work

Acronyms for chemicals used in this work	
$Sr(iPr_3Cp)_2$	Bis(triisoproplycyclopentadienyl) strontium(II)
TEMAT	Tetrakisethylmethylamido titanium(IV)
Sr acac	Strontium acetylacetonate
Pyd	Pyridine
PA	Propylamine
MePT	2-Methyl-2-propanethiol

reaction setup preparations were performed in a nitrogen-filled glovebox, consistent with our earlier report.[6] Due to interactions between the non-polar chains of the precursors and the long hydrocarbon chains of OLA, the precursors dissolved more readily. After dissolution, a 20-fold molar excess of CS_2, relative to the moles of the Sr precursor, was added. The CS_2 reacted with oleylamine to form oleyldithiocarbamic acid, causing the solution to become slightly viscous. Although this solution is somewhat viscous at room temperature, its viscosity decreases when heated above 60 °C and the solution remained homogeneous without any visible particles. Separately, mineral oil in the reaction flask was heated on an argon-purged Schlenk line to the reaction temperature. No visible changes were observed during the heating of the mineral oil. The OLA–CS_2 solution containing the metal precursors was then hot-injected through a syringe into the mineral oil at 375–380 °C (see Fig. S1 for the reaction setup). This step likely caused the breakdown of the metal precursors, forming reactive species, with oleyldithiocarbamic acid serving as the sulfur source, ultimately resulting in the formation of ternary Sr–Ti–S nanocrystals. Upon injection, intense fumes were observed, and the solution immediately turned black, likely due to the nucleation of Sr–Ti–S nanocrystals. The solution was maintained at this temperature for 30 minutes before the heating mantle was turned off and the flask was allowed it to cool naturally to room temperature. No noticeable changes in the reaction solution, such as color or aggregate formation, were observed during the dwell time, however, more sulfur-containing species were observed to condense along the condenser walls as the reaction progressed. After the flask had cooled, the reaction setup was transferred into a glovebox, and the reaction contents were washed with toluene and isopropanol, using toluene as the solvent and isopropanol as the antisolvent. Synthesized in oleylamine, the long-chain tails of the surface ligands provide favorable dispersibility in non-polar solvents. A dark, blackish pellet was collected and redispersed in toluene. The colloidal stability of the nanocrystals in toluene was not optimal as they settled out overnight, possibly due to their morphology, which is discussed in detail later.

It should be noted that Sr–Ti–S crystallizes in an incommensurate structure, differing from stoichiometric $SrTiS_3$, where in the incommensurate structure the TiS_3 units and Sr units share the same '*a*' lattice parameter but have different '*c*' parameters. This results in the formation of Sr_xTiS_3, where '*x*' can vary between 1.05 and 1.22, with 1.143 being the most commonly reported value (see Fig. 2).[15,19,20,22,28–30] Due to the preferential synthesis of the incommensurate phase, the molar ratios of Sr : Ti when preparing reactions were adjusted to 1.1 : 1, and the results from these reactions are discussed below.

The X-ray diffraction (XRD) measurements of the synthesized nanocrystals, as shown in Fig. 3(a), clearly indicate the formation of an $Sr_{8/7}TiS_3$ phase in the nanocrystals. To the best of our knowledge, this represents the lowest synthesis temperature ever reported for Sr_xTiS_3 with significant crystal growth, which could be pivotal for its exploration in various applications. The XRD peaks align best with $Sr_{8/7}TiS_3$, as all the major

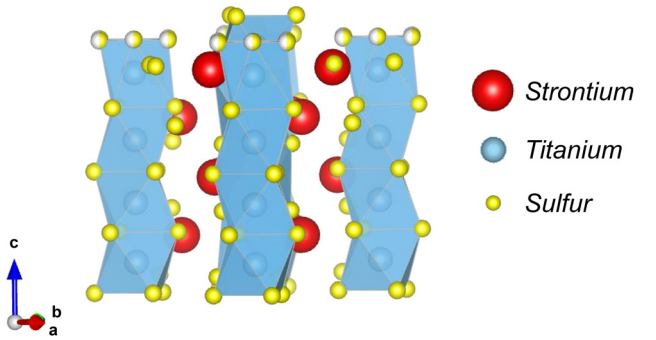

Fig. 2 The crystal structure of $Sr_{8/7}TiS_3$ features face-sharing TiS_3 units and Sr atoms sharing the same '*a*' lattice parameter but differing in their '*c*' parameters.

peaks are present, some of which are unique to $Sr_{8/7}TiS_3$ and not found in other Sr_xTiS_3 phases. However, since the major peaks of other Sr_xTiS_3 phases are also present in $Sr_{8/7}TiS_3$, the presence of small amounts of additional Sr–Ti–S phases cannot be ruled out.[31,32]

Further structural confirmation could have been achieved using Raman spectroscopy; however, the lack of reported Raman spectra for different phases of Sr–Ti–S ternary compounds, combined with our inability to perform this analysis on the nanocrystals, prevented such validation. Attempts to collect Raman spectra proved inconclusive, as our Raman detector became oversaturated with signal, likely due to luminescence from an organic byproduct that was difficult to remove, as is detailed in our previous work.[6] Nevertheless, we confirmed the structure through high-resolution transmission electron microscopy (HRTEM) images, as shown in Fig. 3(b), where the (110), $(\bar{2}43)$, and $(20\bar{1})$ lattice planes of $Sr_{8/7}TiS_3$ are marked. Additionally, Fig. 3(c) presents the fast Fourier transform (FFT) pattern of the $Sr_{8/7}TiS_3$ HRTEM image, displaying multiple spots that represent lattice planes in the nanocrystals, further aiding in the proper assignment of the lattice planes in Fig. 3(b). A more detailed discussion regarding the assignment of these lattice planes is provided in Fig. S2 and S3. To thoroughly confirm the synthesis of $Sr_{8/7}TiS_3$, another set of nanocrystals was inspected for their lattice planes, and their assignment also confirmed the formation of $Sr_{8/7}TiS_3$ (see Fig. S4 and S5). Through scanning transmission electron microscopy-energy dispersive X-ray spectroscopy (STEM-EDX) measurements on the high-angle annual dark-field scanning–transmission electron microscopy (HAADF-STEM) image of the nanocrystals in Fig. 3(d)–(g), we confirmed the presence of only Sr, Ti, and S in the nanocrystals. It should be noted that plasma cleaning of the transmission electron microscopy (TEM) grid prior to performing the STEM-EDX measurements may have skewed any quantitative composition measurements due to uneven sputtering of the elements in the nanocrystals, so we provide these images as a qualitative assessment only. Further supporting the observation of orientation in the nanocrystals, the wide-view TEM images reveal a rod-like morphology as depicted in the inset of Fig. 3(a). The average rod length and rod diameter are estimated to be 40 ± 10 nm and 20 ± 5 nm, respectively. This morphology could be

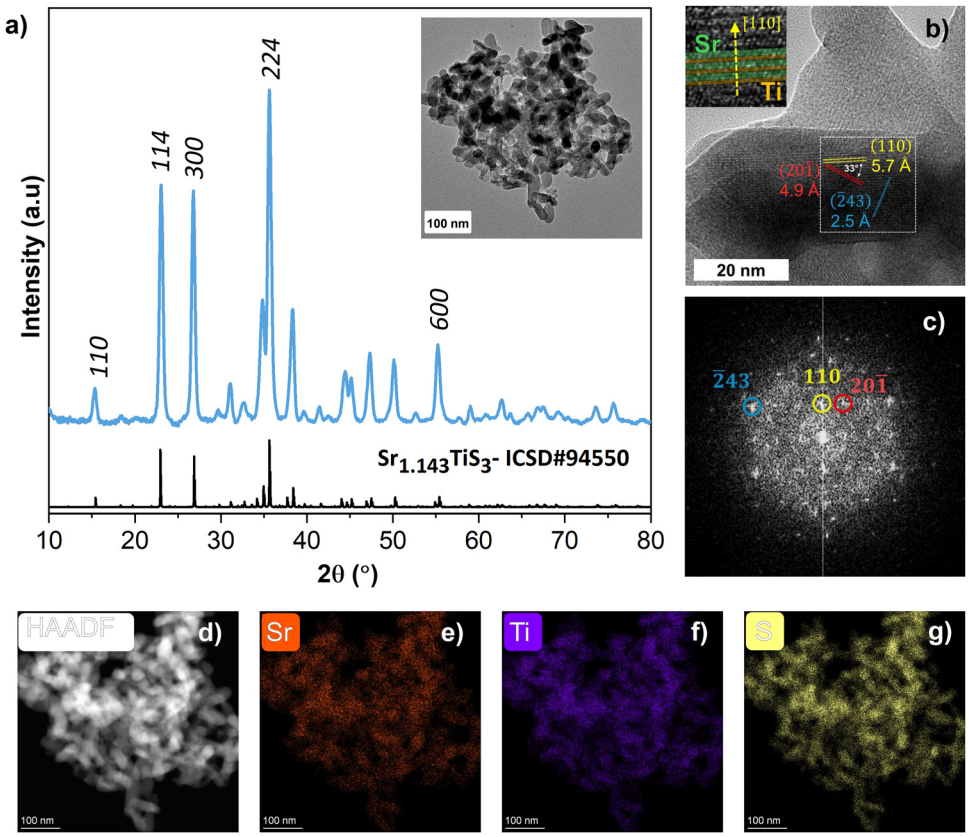

Fig. 3 $Sr_{8/7}TiS_3$ nanocrystals were synthesized through the hot injection of metal precursors, OLA and CS_2 into hot mineral oil at 375–380 °C. (a) XRD pattern, (b) HRTEM image, (c) FFT pattern of the HRTEM image in (b) and (d) HAADF-STEM image of the synthesized nanoparticles, and (e)–(g) elemental maps of Sr, Ti, and S in the synthesized nanocrystals (represents counts). Note: $Sr_{8/7}TiS_3$ has been referred to as $Sr_{1.143}TiS_3$ in the ICSD database.

advantageous for various applications requiring high aspect ratios, large surface areas, and directional electrical properties.

The aforementioned synthesis of $Sr_{8/7}TiS_3$ nanocrystals was achieved at the lowest reported temperature in the literature. However, further investigations allowed us to develop additional protocols without the need for the highest temperatures provided by the use of mineral oil. In this modified approach, we injected the solution containing metal precursors, and oleylamine and CS_2 into hot oleylamine inside the reaction flask at a temperature of 330 °C, which also successfully nucleated $Sr_{8/7}TiS_3$ nanocrystals, as evidenced by the XRD pattern in Fig. 4(a). However, there are some additional broad peak(s) around 20° 2-theta, which we attribute to a residual byproduct of organic residues from the reaction of OLA with CS_2 at high temperatures that was not completely removed during the washing step. Nonetheless, the TEM image in Fig. 4(b) revealed a highly oriented, bundled nanowire-like morphology, with nanocrystals significantly more elongated than those synthesized at 375 °C. The nanowires had an average length of 300 ± 50 nm with a diameter of typically 4–6 nm. This could be due to several reasons: (a) synthesis at a lower temperature may allow for a more controlled growth process. This greater control could result in a much higher aspect ratio, as the precursors break down more slowly, enabling the growth rates of high-energy facets to exceed those of low-energy facets. (b) Without mineral oil, the reaction system has a much higher concentration of ligand. Ligands are used to control nanocrystal growth by selectively binding to certain facets, depending on their surface energies. Mineral oil consists mainly of heavy alkanes and other high-boiling hydrocarbons, which have few or no functional groups for surface binding. By replacing mineral oil with additional OLA, the number of molecules available for surface binding increases significantly, allowing for more selective growth. Nonetheless, this is an interesting result that could be valuable for applications requiring highly oriented thin crystals and should be explored further in future studies. The lattice spacing in the HRTEM image in Fig. 4(c) further supports our identification of the $Sr_{8/7}TiS_3$ phase, with additional details of the lattice plane assignments provided in Fig. S6 and S7. The STEM-EDX analysis in Fig. 4(d)–(g) confirms the presence of only Sr, Ti, and S in the nanocrystals.

In addition to the hot-injection synthesis, a solvothermal reaction was also conducted using metal precursors, CS_2, and oleylamine. In this method, all precursors were placed in a borosilicate vial with the same molar ratios of Sr and Ti precursors and CS_2 as before, along with 3 mL of oleylamine. The vial was sealed and subjected to microwave radiation, with the target temperature set to 300 °C. The XRD pattern of the reaction product showed predominantly SrS, suggesting that the nucleation temperature for $Sr_{8/7}TiS_3$ is likely higher than

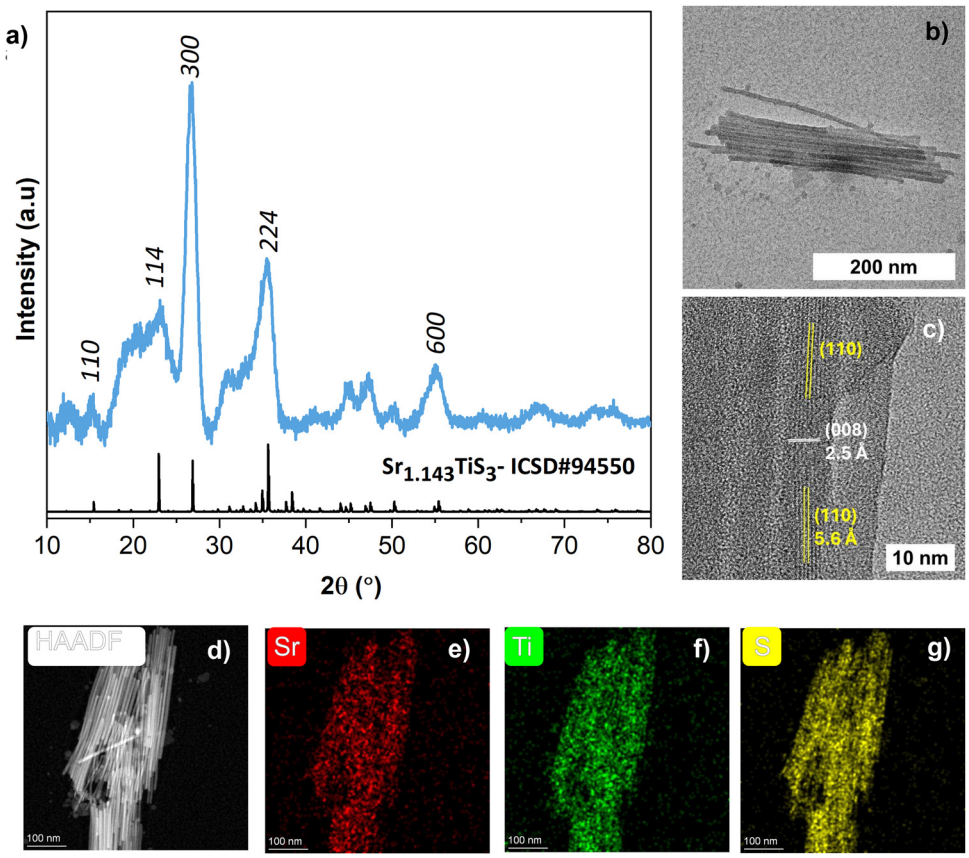

Fig. 4 $Sr_{8/7}TiS_3$ nanocrystals were synthesized through the hot injection of metal precursors, and OLA, and CS_2 into hot OLA at 330 °C. (a) XRD pattern, (b) wide-view TEM image, (c) HRTEM image, (d) HAADF-STEM image of the synthesized nanoparticles, and (e)–(g) elemental maps of Sr, Ti, and S in the synthesized nanocrystals (represents counts). Note: $Sr_{8/7}TiS_3$ has been referred to as $Sr_{1.143}TiS_3$ in the ICSD database.

300 °C. However, in a less controlled experiment using twice the amount of CS_2 as in the previous attempt, the reaction mixture heated rapidly and the pressure rose to 27 bar at 270 °C, resulting in all the peaks of $Sr_{8/7}TiS_3$, along with some secondary peaks indicating the presence of additional phases (see Fig. S8). Due to the inability to safely handle such high-pressure reactions, this experiment was not repeated. Nevertheless, these results suggest that both pressure and temperature play a role in the nucleation of ternary ABS_3 compounds and could be performed safely in traditional autoclaves that can go to much higher pressures than 30 bar.

One limitation of all the previously discussed methods is their reliance on the expensive $Sr(iPr_3Cp)_2$ as the strontium precursor. Therefore, it would be advantageous to synthesize Sr–Ti–S ternary nanocrystals using more cost-effective precursors. In this regard, we attempted the hot injection synthesis of Sr_xTiS_3 nanocrystals using SrS and Sr dibutyldithiocarbamate precursors. However, both attempts resulted in the formation of binary phases rather than the desired ternary compound. The methods used and the resulting XRD patterns are provided in Fig. S9 and S10. A likely reason for these unsuccessful attempts could be the limited intermixing of Sr and Ti precursors before injection in these cases, which could be addressed in future studies.

Synthesis of $Sr_{8/7}TiS_3$ film

Although a film can ideally be synthesized from $Sr_{8/7}TiS_3$ nanocrystals, this approach was not pursued because the nanocrystals exhibited poor colloidal stability in common solvents, possibly due to inadequate ligand coverage and/or large nanocrystal sizes preventing suitable suspension of the nanocrystals. Instead, we explored the synthesis of thin films through molecular precursor routes, where Sr and Ti precursors were dissolved in appropriate solvents along with a sulfur source, forming metal–sulfur bonded complexes. To the best of our knowledge, this represents the first reported attempt to synthesize a solution-processed thin film of Sr_xTiS_3. The only other reported thin film was by Shuhaib *et al.*,[19] who deposited a thin film of $SrTiO_3$ through magnetron sputtering and subsequently sulfurized it using CS_2 in a sealed ampule or a flow reactor at 900 °C for multiple hours. However, the resulting film was significantly porous, contained high levels of oxygen and carbon, and exhibited a bandgap of 1.1 eV, which is considerably higher than previously reported values.[19]

We have previously published articles on the synthesis of the chalcogenide perovskite $BaZrS_3$, noting that the use of highly reactive precursors is crucial for synthesizing it at moderate temperatures (<600 °C).[14] Additionally, Ti, along with Zr and Hf, are among the most oxophilic elements in the periodic

Table 2 List of all the molecular precursor solutions used for the solution-processed thin film synthesis of $Sr_{8/7}TiS_3$

Mixed metal precursor solutions used in this work		Synthesis result
M1	$Sr(iPr_3Cp)_2$ + TEMAT + CS_2 + Pyd	$Sr_{8/7}TiS_3$
M2	$Sr(iPr_3Cp)_2$ + CS_2 + Pyd TEMAT + MePT + Pyd	$Sr_{8/7}TiS_3$
M3	$Sr(iPr_3Cp)_2$ + TEMAT + MePT + CS_2 + Pyd	$Sr_{8/7}TiS_3$
M4	SrS + CS_2 + PA + Pyd TEMAT + CS_2 + Pyd	$Sr_{8/7}TiS_3$ (and TiS_3 secondary phase)
M5	Sr acac + Ti isopropoxide + CS_2 + PA + Pyd	$Sr_{8/7}TiS_3$ (and oxide secondary phases)

table.[24,25] Therefore, it is advisable to either use oxygen-free metal precursors or employ an oxygen sink during synthesis. Drawing inspiration from these principles, this study explores a variety of precursors, including metal acetylacetonates, metal sulfides, and reactive organometallic/metal–organic precursors. Table 2 summarizes the five approaches we employed, along with the corresponding precursors, sulfur sources, and solvents used for dissolution.

In our first approach, M1, we utilized the organometallic precursor $Sr(iPr_3Cp)_2$ and the metal–organic precursor tetrakis(ethylmethylamido) titanium (TEMAT). These were reacted with CS_2, which inserted into the metal–carbon and metal–nitrogen bonds, respectively, to form Sr dithiocarboxylate and Ti dithiocarbamate species. These species were co-soluble in pyridine due to their polar nature. Although attempts were made to dissolve them in other polar solvents such as *N*,*N*-dimethyl formamide (DMF), dimethyl sulfoxide (DMSO), and *N*-methyl-2-pyrrolidone (NMP), these efforts were unsuccessful. This approach is adapted from our previous study on $BaZrS_3$, and the CS_2 insertion chemistry documented in the literature.[33] The resulting ink was blade-coated and annealed on a hotplate in an argon-filled glovebox, forming an amorphous Sr–Ti–S matrix as the film. The film was then sealed in an ampule with sulfur and HfH_2 and subjected to sulfurization. As explained in our previous study, at elevated temperatures (>500 °C), HfH_2 reacts with sulfur vapor to form HfS_3, generating *in situ* H_2S, which acts as both an oxygen sink and shuttle to remove bulk oxygen impurities from the film.[25] The sulfurization was performed at 575 °C for 2 h, yielding $Sr_{8/7}TiS_3$, as confirmed by XRD and Raman spectroscopy.

Due to the similarity in diffraction patterns among different Sr_xTiS_3 structures, assigning a specific structure to the observed pattern is challenging. However, the XRD pattern matched best with $Sr_{8/7}TiS_3$ compared to other alternatives (see Fig. 5a). Raman analysis (Fig. 5b) also aligned with the only other reported Raman spectrum for $Sr_{8/7}TiS_3$ by Shuhaib *et al.*[19] The Raman spectrum closely resembles that of $BaTiS_3$, which has a similar hexagonal, $BaNiO_3$-type structure with peaks at 200 and 370 cm^{-1}, further supporting the successful synthesis of $Sr_{8/7}TiS_3$.[34] Sulfurization for an extended duration of 16 h did not result in significantly greater crystal orientation or additional secondary impurities compared to the sample sulfurized for 2 h (see Fig. S11). The Kubelka–Munk transformation of the diffuse reflectance spectrum revealed a direct bandgap of 0.95 eV for Sr_xTiS_3, consistent with previously reported values.[19,21]

Fig. 5d–g present the scanning electron microscopy-energy dispersive X-ray spectroscopy (SEM-EDX) analysis of the film, which shows that while the film appears macroscopically homogeneous, it contains some void spaces rather than forming a smooth, continuous layer. Nonetheless, EDX analysis confirms the presence of Sr, Ti, and S in the film, with possible minor oxide impurities and a slightly Sr and S deficient composition (see Fig. S12 for detailed analysis). To further investigate the structure and composition, a thin lamella of the film was prepared using a focused ion beam (FIB) and analyzed using *via* STEM. HRTEM analysis of the lamella (Fig. 6a) reveals the (114) and (110) lattice planes of $Sr_{8/7}TiS_3$, with additional details provided in the FFT image of the lamella (see Fig. S13–S15). HAADF-STEM and STEM-EDX images (Fig. 6b–e, Fig. S16, and S17) indicate that the lamella primarily consists of Sr, Ti, and S, but significant amounts of oxides are present on the surfaces. It is unclear whether these oxides formed during synthesis or if the lamella oxidized during post-synthesis processing and handling, as HfH_2 is expected to remove major oxide impurities during synthesis. However, in the grain centers, where minimal oxygen is present, the Sr : Ti : S ratios fall within the expected range, albeit with a slight S deficiency (see Fig. S18). The slight sulfur deficiency may be attributed to the oxygen content in the grains. As shown in Fig. S17, the lamella exhibits significant porosity, suggesting that longer sulfurization times may be required to sinter the grains and achieve a more compact film. However, this optimization was not pursued in this study, as the primary focus was to establish methods for synthesizing $Sr_{8/7}TiS_3$.

In our M2 and M3 approaches, we again utilized the organometallic precursor $Sr(iPr_3Cp)_2$ and the metal–organic precursor TEMAT. However, in these approaches, we aimed to create an ink containing dissolved Sr and Ti thiolates in a solvent. To achieve this, we reacted $Sr(iPr_3Cp)_2$ with various thiols, including primary thiols such as 2-methyl-2-propanethiol, propanethiol, and ethanedithiol. Unfortunately, the resulting thiolates were insoluble in commonly used primary amines (*e.g.*, propylamine, butylamine, ethylenediamine, and hexylamine) as well as in other polar and non-polar solvents such as pyridine, toluene, and hexane.

In approach M2, we reacted TEMAT with 2-methyl-2-propanethiol to form a titanium 2-methyl-2-propanethiolate species, which was found to be soluble in pyridine. Although this exact reaction has not been studied previously, a similar reaction involving tetrakis(dimethylamido)titanium and 2-methyl-2-propanethiol resulted in a titanium thiolate species, and the same outcome is expected here.[35] Separately, $Sr(iPr_3Cp)_2$ was reacted with a stoichiometric amount of CS_2 (1 mole of $Sr(iPr_3Cp)_2$ with 2 moles of CS_2), forming a Sr dithiocarboxylate species that also dissolved in pyridine. The resulting Sr and Ti solutions in pyridine were then mixed, yielding a fully dissolved solution of Sr and Ti. This solution was blade-coated and sulfurized in an ampule with sulfur and HfH_2, resulting in the formation of $Sr_{8/7}TiS_3$, as confirmed by XRD (see Fig. S19).

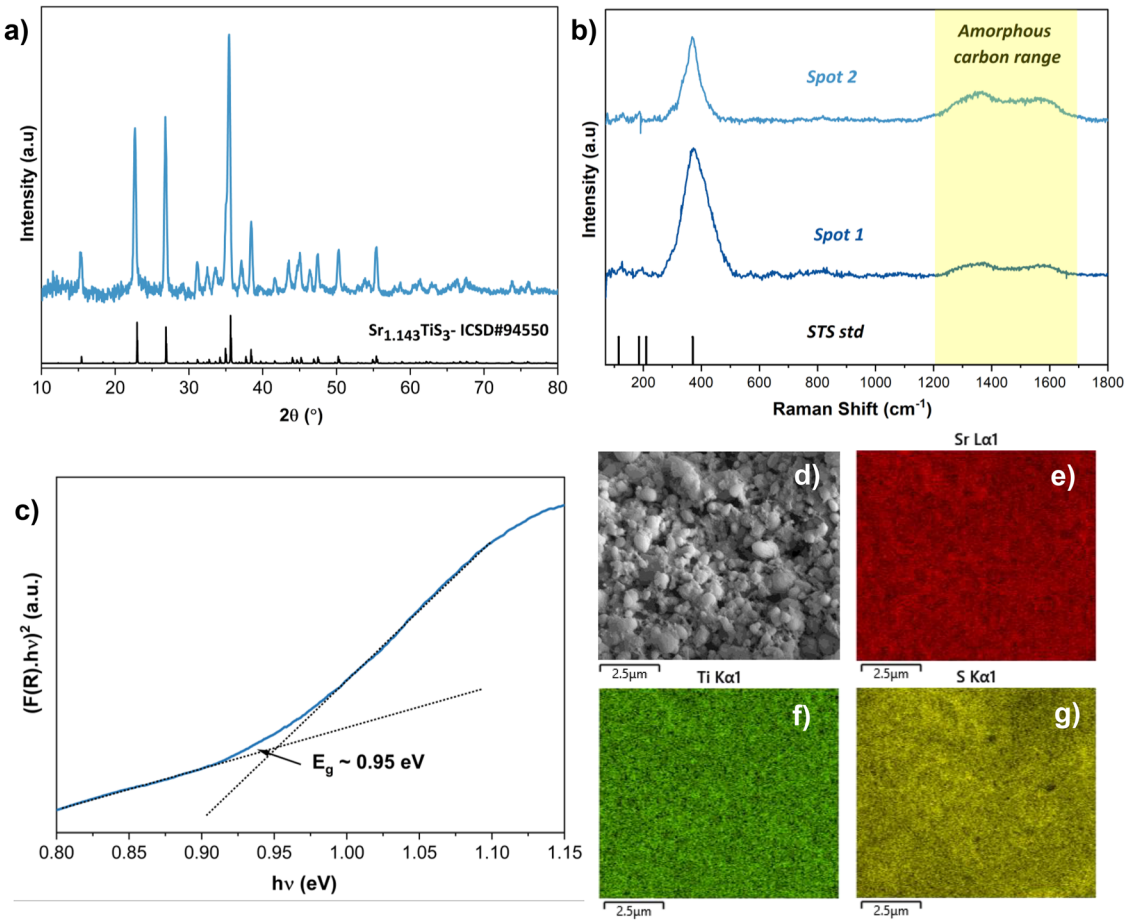

Fig. 5 $Sr_{8/7}TiS_3$ thin film synthesized using the solution described as M1 and sulfurized at 575 °C for 2 h. (a) XRD pattern, (b) Raman spectrum, (c) Kubelka–Munk transformation of the diffuse reflectance spectrum, (d) SEM image of the fabricated film, and (e)–(g) elemental maps of Sr, Ti, and S in the film. Note: $Sr_{8/7}TiS_3$ has been referred to as $Sr_{1.143}TiS_3$ in the ICSD database. Raman spectrum of $Sr_{8/7}TiS_3$ reported by Shuhaib *et al.*[19] has been used for comparison.

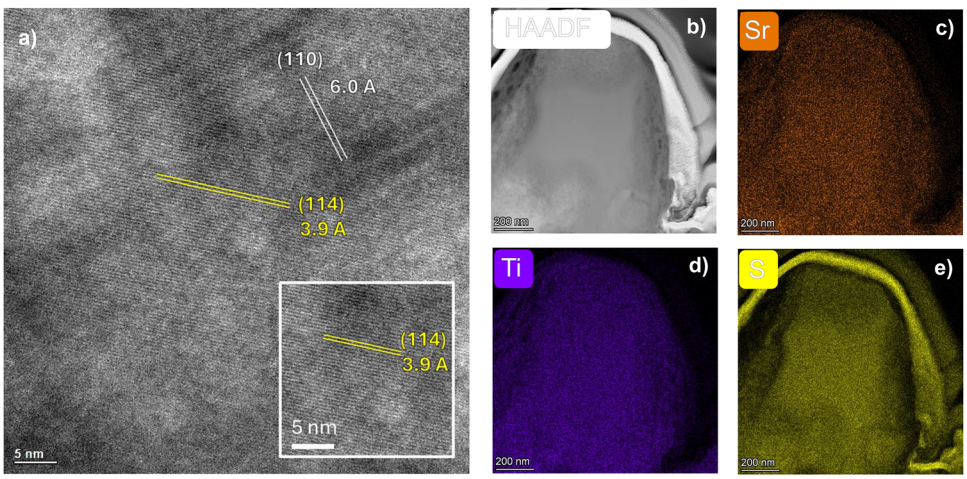

Fig. 6 $Sr_{8/7}TiS_3$ thin film synthesized using the solution described as M1 and sulfurized at 575 °C for 2 h. (a) HRTEM image, (b) HAADF-STEM image of a lamella from the fabricated film, and (c)–(e) elemental maps of Sr, Ti, and S in the film lamella. 30–50 nm of Pt layer was deposited on the film before the FIB.

In approach M3, $Sr(iPr_3Cp)_2$ and TEMAT were first reacted with 2-methyl-2-propanethiol to form metal thiolate species. These species were then reacted with an excess of CS_2, which inserted into the metal–sulfur bonds of the thiolates, forming

strontium and titanium trithiocarbonate species.[14] These species were co-soluble in pyridine, resulting in a fully dissolved solution. The solution was blade-coated and sulfurized with sulfur and HfH_2 at 575 °C for 2 h, yielding phase-pure $Sr_{8/7}TiS_3$, as confirmed by XRD measurements (see Fig. S20).

All previous approaches to synthesizing $Sr_{8/7}TiS_3$ relied on the expensive $Sr(iPr_3Cp)_2$ precursor. Therefore, we aimed to develop solution-processing methods using more common precursors. In the M4 approach, we dissolved SrS in a mixture of propylamine, CS_2, and pyridine. Propylamine and CS_2 react to form propyldithiocarbamic acid, which is soluble in pyridine.[14] When SrS is added to this mixture, the reactive –CSSH group of propyldithiocarbamic acid reacts with SrS, forming a Sr dithiocarbamate species that dissolves in pyridine. This process yields a dissolved solution of SrS in the bulk solvent pyridine. Separately, TEMAT was reacted with CS_2 to form a Ti dithiocarbamate species, to which the SrS solution was added. This resulted in a hybrid route with a dissolved Sr precursor but a slurry of the Ti precursor in pyridine. The resulting solution was drop-cast and sulfurized with sulfur and HfH_2 at 575 °C for 2 h. Fig. S21 confirmed the formation of the $Sr_{8/7}TiS_3$ phase, along with minor impurities of TiS_3, likely due to the slurry nature of the solution rather than a fully dissolved, homogeneous mixture. Future work could explore identifying a Ti precursor that dissolves compatibly with SrS in this chemistry.

Lastly, in our M5 approach, we utilized oxygen-containing precursors, like acetylacetonates, which are commonly employed for the synthesis of other chalcogenides, such as $Cu(In,Ga)(S,Se)_2$.[36] For strontium, we used strontium acetylacetonate, and for titanium, we used titanium isopropoxide. These precursors were co-dissolved in propylamine–CS_2–pyridine. We discussed this chemistry in our previous publication, where it was used to synthesize $BaZrS_3$ and $BaTiS_3$.[14] The resulting solution was coated and sulfurized with sulfur and HfH_2 at 575 °C for 2 h. However, this approach resulted in significant oxide impurities alongside the $Sr_{8/7}TiS_3$ phase, as shown in Fig. S22. While this method employs the most cost-effective precursors, the issue of oxide formation remains a challenge. This could potentially be addressed by exploring longer sulfurization times, slightly higher temperatures, or modifying the oxygen sink used in these reactions.

Overall, our five approaches provide a comprehensive set of solution-processing methods to synthesize thin films of Sr_xTiS_3, a feat that has not been previously achieved. These methods hold promise for exploring this exciting material for various applications.

Shuhaib *et al.* previously demonstrated the high thermal stability of Sr_xTiS_3 through thermogravimetric studies, showing that it remains stable under argon at temperatures up to 1200 °C.[19] However, no studies have been conducted on the air or water stability of Sr_xTiS_3, despite its potential use in applications where exposure to air or water-containing environments is likely. To address this, we evaluated the air and water stability of the $Sr_{8/7}TiS_3$ film synthesized *via* our M1 route.

For air stability testing, the film was stored in ambient air for over a month, after which the XRD pattern was collected again. We observed that all major peaks remained intact; however, the relative intensity (normalized with respect to peak at ~35.7° 2-theta) of the peak around 15° 2-theta, corresponding to the (110) plane, increased over time (demonstrated in Fig. 7a). The 15° is also the most dominant peak of $Sr_{1.145}TiS_3$, so at this stage, we assume that some structural rearrangement occurs upon prolonged exposure to air. However, this phenomenon should be studied in more detail in the future to better understand its origin.

To assess water stability, the synthesized $Sr_{8/7}TiS_3$ film was thoroughly rinsed with running distilled water for 5 minutes. The XRD pattern collected afterward showed no distinct changes, indicating the material's high stability in the presence of water (see Fig. 7b). These findings highlight the robustness of $Sr_{8/7}TiS_3$ under both air and water exposure, which is promising for its potential use in real-world applications.

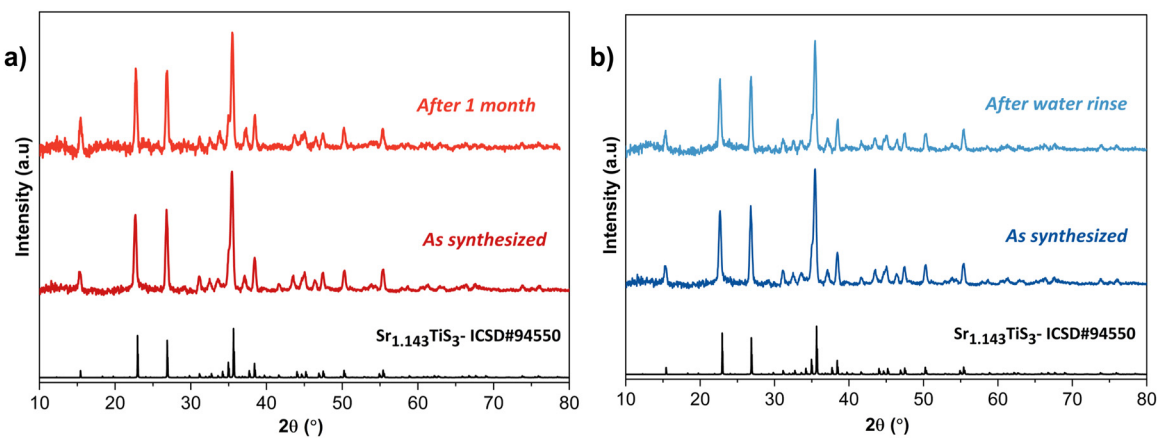

Fig. 7 $Sr_{8/7}TiS_3$ thin film synthesized using the solution described as M1 and sulfurized at 575 °C for 2 h. (a) Comparison of the XRD patterns after storing the sample in air for over 1 month, and (b) comparison of the XRD patterns after rinsing the film for approximately 5 minutes. Note: $Sr_{8/7}TiS_3$ has been referred to as $Sr_{1.143}TiS_3$ in the ICSD database.

Synthesis of $Sr_{8/7}TiS_3$ powder

In addition to nanocrystals and thin films, we aimed to explore whether bulk Sr_xTiS_3 powder could be synthesized at temperatures below 600 °C using stable metal precursors such as metal sulfides. To test this, we sealed SrS and TiS_2 powders in an ampule along with excess sulfur and sulfurized the mixture at 575 °C for 3 days. Although the powders were well mixed, they were not ground prior to sulfurization. The XRD pattern in Fig. S23 revealed that $Sr_{8/7}TiS_3$ represents a significant phase, alongside $Sr_{1.145}TiS_3$, SrS, and Ti–S phases. As noted previously, all the reflections of $Sr_{1.145}TiS_3$ overlap with those of $Sr_{8/7}TiS_3$, with $Sr_{8/7}TiS_3$ exhibiting additional reflections. This conclusion is based on the relative intensities of the peaks, which correspond more closely to $Sr_{1.145}TiS_3$ than to $Sr_{8/7}TiS_3$.[31,32] A similar reaction was attempted using Ti metal instead of TiS_2, which also resulted in a mixture of $Sr_{8/7}TiS_3$, $Sr_{1.145}TiS_3$, SrS, and Ti–S phases (see Fig. S24). It is rather intriguing that, despite the initial precursors being well mixed but not ground or ball-milled, and with neither Sr–S nor Ti–S known to have any liquid phases at the operating temperatures to facilitate mass transfer, the final product still contains significant ternary phases. It is possible that given the Sr–Ti–S composition in this experiment, we may be approaching a eutectic point granting us access to a liquid phase that bypasses the diffusion barriers necessary for the formation of the ternary phase.

When the sulfurization of SrS and TiS_2 was performed with both sulfur and iodine, we again observed the formation of $Sr_{8/7}TiS_3$ alongside secondary impurities of SrI_2, though the ternary phase was much more dominant, as shown in the XRD pattern in Fig. S25. Iodine, a well-known vapor transport agent,[37] facilitated the formation of Sr–Ti–S ternary phases, indicating that mass transport remains a limiting factor in bulk synthesis when starting with bulk powder precursors. In contrast, the intermixing of molecular Sr and Ti precursors likely enables the phase-pure synthesis of $Sr_{8/7}TiS_3$ films at the same temperature without the need for a transport agent.

Conclusions

Chalcogenide perovskites have emerged as an exciting class of semiconductor materials being explored for various optoelectronic applications. In this study, we focused on Sr_xTiS_3, which has previously demonstrated promising birefringence alongside other intriguing properties. However, the synthesis temperatures required for conventional solid-state routes remain prohibitively high. To address this, we explored solution-processing techniques to synthesize Sr_xTiS_3 nanocrystals and thin films through molecular precursor routes.

We successfully achieved phase-pure, rod-shaped nanocrystals of Sr_xTiS_3 *via* a hot-injection procedure at temperatures between 330–380 °C. The rod-like morphology of these nanocrystals could be leveraged for a variety of interesting applications. Furthermore, we developed five solution-chemistry strategies to deposit and fabricate thin films of Sr_xTiS_3. Diffraction measurements confirmed the formation of the $Sr_{8/7}TiS_3$ phase, which exhibits a direct bandgap of 0.95 eV. EDX analysis revealed uniform distribution of Sr, Ti, and S, though the composition was slightly sulfur-deficient, with oxygen potentially occupying some sulfur sites. Stability studies demonstrated that $Sr_{8/7}TiS_3$ exhibits high stability in both air and water, further supporting its potential for exploration in a wide range of applications.

Experimental details

Materials and characterization

Carbon disulfide (CS_2, anhydrous, >99%), pyridine (Pyd, anhydrous, 99.8%), *N*,*N* dimethyl formamide (DMF, anhydrous, 99.8%), thiourea (TU, ACS Reagent, >99%), sulfur flakes (>99.99%), molecular sieves (type 3A, bead size 8–12 mesh), alumina dispersed in isopropanol (20 wt%), tetrakisethylmethylamido titanium(IV) (TEMAT, >99.999%), oleylamine (technical grade, 70%; OLA), toluene (anhydrous, 99.8%), isopropanol (anhydrous, 99.5%; IPA), calcium hydride (95%; CaH_2) and 2-methyl-2-propanethiol (99%) were purchased from Sigma Aldrich. Bis(triisoproplycyclopentadienyl)strontium(II) ($Sr(iPr_3Cp)_2$, 98%), strontium acetylacetonate hydrate, titanium(IV) isopropoxide (min. 97%) and strontium sulfide (99.9%) were purchased from STREM chemicals. Hafnium hydride (99.9%) was purchased from Nano Research Elements. Borosilicate glass ampules were procured from Chemglass. High purity mineral oil was purchased from Fisher Scientific. Alkali-free Eagle XG (EXG) glass substrates were obtained from Stemmerich.

All materials listed as anhydrous were used as received. Any other materials not listed in the purification section below were used as received.

Purification of materials prior to use

Before experimental use, many of the materials underwent various purification steps. Molecular sieves, which are synthetic crystalline aluminosilicate beads with a pore size of 3 Å, were dried overnight *in vacuo* at 150 °C prior to use. Glassware used during purification, drying, or for storage after these processes was dried in a vacuum oven under partial vacuum (~800 mbar) in an argon atmosphere at 150 °C for at least 30 minutes before use. The purification and/or drying steps for the various materials are as follows:

Oleylamine purification process:

(1) Freeze–pump–thaw (FPT) cycles:

~250 mL of OLA was transferred to a 500 mL round-bottom flask (RBF) in an N_2-filled glovebox. The flask was sealed, moved to an Ar-purged Schlenk line, and purged three times *via* vacuum/Ar cycles. Three FPT cycles were performed to remove dissolved gases:

(a) the OLA was frozen using liquid nitrogen.

(b) It was then melted with gentle heating using a heat gun while maintaining dynamic vacuum (~150–350 mtorr).

(2) Drying with CaH_2:

After the FPT cycles, ~2.5 g of CaH_2 (1 g per 100 mL OLA) and a stir bar were added in the glovebox. The flask was

returned to the Schlenk line, purged three times, and stirred under vacuum at room temperature for 12–16 h. It was then heated to 200 °C (measured at the flask surface) for 2 h under vacuum.

(3) Vacuum evaporation:

The OLA was decanted into a 250 mL RBF in the glovebox, minimizing CaH_2 transfer. The evaporation setup was purged three times with Ar, and the collection flask was heated with a heat gun to ensure dryness. Evaporation was performed under reduced pressure (~200–400 mtorr) with the heating mantle set to 200–280 °C and heating tape at 30–50% power. The condensed vapor was collected as OLA liquid for further use.

(4) Storage:

The purified OLA was stored over molecular sieves for at least a day before use and remained stored over the same sieves during its usage.

All chemicals were stored in nitrogen-filled gloveboxes and handled exclusively within the gloveboxes. Solvents without a sure-seal cap were stored over molecular sieves for several days prior to use. Thiourea was purified through two recrystallization steps using 18.2 MΩ deionized water and then dried under vacuum overnight. Strontium acetylacetonate was vacuum-dried at 150 °C overnight before use. Sulfur flakes were finely ground inside a nitrogen-filled glovebox and subsequently vacuum-dried overnight at room temperature *via* Schlenk line techniques.

All molecular precursor films in this study were deposited on alumina-coated EXG glass. Prior to alumina deposition, the EXG glass was thoroughly rinsed with deionized (DI) water, 2-propanol, and methanol, followed by sonication in an Alconox bath and DI water. Subsequently, the glass was cleaned in a UV-ozone cleaner for 30 minutes. A commercial alumina nanoparticle solution was diluted for deposition by mixing 0.2 mL of the commercial solution with 1.8 mL of isopropanol. The resulting solution was spin-coated onto the cleaned EXG glass at 1000 rpm for 1 minute, followed by annealing at 100 °C for 1 minute and then at 500 °C for 30 minutes. All thin film samples were stored in ambient air for an average of 1–2 days between characterization steps. The samples in Fig. 7 were stored in air for a month to assess stability.

Raman spectroscopy was performed using a Horiba/Jobin-Yvon HR800 Raman spectrometer with a 632.8 nm excitation laser wavelength.

XRD was conducted using a Rigaku SmartLab diffractometer under ambient conditions, employing parallel beam geometry with an incident beam angle of 0.5 degrees. Data collection utilized a Cu Kα source (λ = 1.5406 Å) operated at 40 kV and 44 mA.

SEM and SEM-EDX measurements were performed using the Quanta 3D FEG equipped with an Everhart Thornley detector. The measurements were carried out at an accelerating voltage of 10 kV with a working distance of 10 mm. Pt was sputter deposited on the films for easier SEM imaging.

Reflectance data were obtained employing a PerkinElmer Lambda 950 spectrometer equipped with an integrating sphere.

TEM samples from the thin films were prepared using a Ga-FIB on an FEI HELIOS G5 UX Dual Beam FIB-SEM. The samples were exposed to ambient air for an average of 1–2 weeks between synthesis and fibbing. Nanocrystal samples were prepared *via* drop-casting on a 300 mesh Cu TEM grid and drying off the solvent in air. TEM, STEM-HAADF imaging, and STEM-EDX analysis were performed on an FEI Talos F200i scanning/transmission electron microscope (S/TEM) at an accelerating voltage of 200 kV.

Synthesis of Sr_xTiS_3 nanocrystals

Before use, all glassware intended for nanoparticle reactions was dried at 150 °C in a vacuum oven under partial vacuum (~800 mbar) in an argon atmosphere for at least 30 minutes. A hot-injection procedure was employed for these reactions, with all reaction setup and post-synthesis workup conducted in an N_2-filled glovebox.

For the hot-injection method, 0.16 mmol of $Sr(iPr_3Cp)_2$ and 0.145 mmol of TEMAT precursors were added to a borosilicate vial along with 2 mL of OLA. The mixture was stirred for several hours, resulting in fully dissolved metal precursors in OLA. Subsequently, a ~20-fold molar excess of CS_2 (300 μL) was added to the vial and stirred. After the addition of CS_2, the solution became slightly viscous.

In a separate three-neck flask, 3 mL of a mineral oil or OLA mixture was added. The flask was then sealed with an Allihn condenser, an *in situ* thermocouple, and a rubber septum before being removed from the glovebox and attached to an Ar-purged Schlenk line. A schematic of the typical setup used for hot-injection reactions is shown in Fig. S1.

Meanwhile, the dissolved metal precursors, OLA, and CS_2 solution were transferred to a single-neck round-bottom flask, sealed with a rubber septum, and brought out of the glovebox. Due to the high viscosity of the solution, it was heated to 60 °C to reduce its viscosity, making it easier to draw into a syringe. The Schlenk line port was purged three times *via* Ar/vacuum cycles, with the vacuum reaching <150 mtorr on the final cycle. The reaction flask was then opened to the Ar flow from the Schlenk line and heated to a set point of 330–380 °C.

Once the temperature stabilized, a syringe with a stainless steel needle was purged multiple times with N_2 to remove trapped air. The CS_2 and OLA solution was drawn into the syringe from the single-neck flask and injected into the heated mineral oil/OLA mixture. The prescribed dwell time (typically 30 minutes) began upon injection of the precursors into the hot solvent. After the dwell time elapsed, the flask was allowed to cool naturally before being returned to the N_2-filled glovebox for nanoparticle washing.

To wash the nanoparticles, 1–3 mL of toluene was added to the reaction mixture and vortex-mixed, followed by the addition of 12–18 mL of isopropanol (IPA) and another vortex mix. The mixture was then centrifuged for 5 minutes at 14 000 rpm, resulting in a dark pellet and a yellowish supernatant of varying opaqueness. This washing process was repeated two to three times, depending on the amount of gel-like species (a byproduct of OLA and CS_2 at high temperatures) present. The gel was typically removed and discarded between washing cycles. After washing, the nanoparticles were suspended in toluene and stored

in the N_2-filled glovebox for an average of 1–2 days between characterizations.

Thin film synthesis

All chemical storage, solution preparation, thin film coating, and sample handling were conducted inside nitrogen- and ultra-high purity (UHP 99.999%) argon-sourced gloveboxes. In all instances, unless specified, the solutions were blade-coated using an automated blade coater at a speed of 15 mm per second with a single pass, followed by annealing at 350 °C for 2 minutes on a hot plate and cooling for 1 minute. The coating was repeated 6–8 times on alumina-coated Eagle XG substrates. Without any exposure to air, Sr–Ti–S were cut into 25 mm by 7–8 mm strips in a glovebox and placed in 5 mL borosilicate glass ampules. The samples, sulfur powder, and HfH_2 powder were loaded into the ampule inside the glove box as per our previous work[25] and then connected to a red rubber tubing with a Teflon vacuum valve at the end. The ampules were then sealed on the Schlenk line with UHP argon as the purging gas.

Subsequently, the ampules were heated in a refractory furnace to the desired temperature and cooled naturally under a slow argon flow.

M1: a 0.2 M solution of $Sr(iPr_3Cp)_2$ and TEMAT was prepared with the Sr : Ti molar ratio of 1.1 : 1 and pyridine : CS_2 molar ratio of 1 : 4. The solution was stirred at 35 °C. The metal precursors were added first, followed by CS_2 and finally pyridine. The solution dissolved within 1 h. The films were blade-coated as discussed earlier, sealed in an ampule with HfH_2 and sulfur, and heated at 575 °C 2 h to synthesize $Sr_{1.143}TiS_3$.

M2: a 0.2 M solution of $Sr(iPr_3Cp)_2$ was prepared by using twice the molar amount of CS_2 relative to the Sr precursor, with pyridine as the bulk solvent. The strontium precursor was added first, followed by CS_2, and finally pyridine. The solution was stirred at 35 °C and dissolved within 1 h. Separately, a 0.2 M solution of TEMAT was prepared so that the Sr : Ti molar ratio is 1.1 : 1, using four times the molar amount of MePT relative to TEMAT and pyridine as the bulk solvent. The titanium precursor was added first, followed by MePT, and finally pyridine. This solution was also stirred at 35 °C and dissolved within 1 h. The entire volumes of strontium and titanium solutions were then mixed together. The films were blade-coated as discussed earlier, sealed in an ampule with HfH_2 and sulfur, and heated at 575 °C 2 h to synthesize $Sr_{1.143}TiS_3$.

M3: a 0.1 M solution of $Sr(iPr_3Cp)_2$ and TEMAT was prepared with the Sr : Ti molar ratio of 1.1 : 1 and pyridine : 2-methyl-2-propanethiol : CS_2 molar ratio of 1 : 1 : 4. The solution was stirred at 35 °C. The metal precursors were added first, followed by 2-methyl-2-propanethiol, and then CS_2 and finally pyridine. The solution dissolved within 1 h. The films were blade-coated as discussed earlier, sealed in an ampule with HfH_2 and sulfur, and heated at 575 °C 2 h to synthesize $Sr_{1.143}TiS_3$.

M4: a 0.2 M solution of SrS was prepared with a propylamine : CS_2 : pyridine molar ratio of 1 : 1 : 0.73, stirred overnight at 35 °C. Separately, a 0.2 M solution of TEMAT was prepared so that the Sr : Ti molar ratio is 1.1 : 1 and pyridine : CS_2 molar ratio of 1 : 4. The titanium precursor was added first, followed by CS_2, and finally pyridine. This solution was also stirred at 35 °C. The entire volumes of strontium and titanium solutions were then mixed together. The films were drop casted, sealed in an ampule with HfH_2 and sulfur, and heated at 575 °C 2 h to synthesize $Sr_{1.143}TiS_3$.

M5: as purchased strontium acetylacetonate was dried under vacuum at 150 °C overnight and used. Dried strontium acetylacetonate and titanium isopropoxide were used. A solution with 0.2 M total metal concentration and Sr : Ti ratio 1.2 : 1 was prepared with propylamine : CS_2 : pyridine molar ratio of 1 : 1 : 0.73, stirred overnight at 35 °C. The metal precursors were added first, followed by propylamine, then CS_2, and finally pyridine. The solution dissolved within 1 h of stirring.

Solid state synthesis

Attempt 1: a mixture of 0.11 mmol of SrS, 0.1 mmol of TiS_2, 6 mg of sulfur, and 2 mg of I_2 was loaded into a 10 mL ampule. The ampule was flame-sealed on the Schlenk line after purging the headspace. The sulfurization process was carried out at 575 °C for 3 days.

Attempt 2: a mixture of 0.11 mmol of SrS, 0.1 mmol of TiS_2, and 10 mg of sulfur was loaded into a 10 mL ampule. The ampule was flame-sealed on the Schlenk line after purging the headspace. The sulfurization process was conducted at 575 °C for 3 days.

Attempt 3: a mixture of 0.11 mmol of SrS, 0.1 mmol of Ti, and 15 mg of sulfur was loaded into a 10 mL ampule. The ampule was flame-sealed on the Schlenk line after purging the headspace. The sulfurization process was carried out at 575 °C for 3 days.

Safety and scalability considerations

The synthesis of semiconductor materials often involves working with hazardous substances, including toxic gases and reactive chemicals. A thorough understanding of the proper storage and handling procedures is critical prior to working with these materials. In this study, the insitu generated H_2S was handled with strict safety protocols. All ampules were opened exclusively inside fume hoods to avoid exposure. The organometallic precursor tetrakis ethyl methyl amido titanium (TEMAT) used in this study is highly flammable and toxic (NFPA rating – health: 4 and flammability: 4). It was stored and handled inside N_2 filled gloveboxes and the boxes were continuously purged while handling the precursors, to avoid any exposure. All solvents and chemicals, including CS_2, used in this study were handled inside glove boxes and fume hoods with appropriate PPE.

Regarding scalability, both H_2S and organometallic TEMAT are commonly used in chemical vapor deposition (CVD) processes and pose no significant barrier.[38,39] However, the biggest challenge lies in translating the current ampule-based batch synthesis to continuous fabrication while maintaining an oxygen-free environment. This would require innovative engineering and safety efforts. Nonetheless, this study provides a

solid foundation for materials synthesis and a basis for future research efforts to overcome these challenges.

Author contributions

K. C. Vincent: writing – original draft, writing – review & editing, validation, methodology, investigation, formal analysis, data curation, visualization, conceptualization. S. Agarwal: writing – original draft, writing – review & editing, validation, methodology, investigation, formal analysis, data curation, visualization, conceptualization. S. Rodriguez: writing – review & editing, validation, methodology, investigation, formal analysis, data curation. D. C. Hayes: formal analysis, writing – review & editing. K. Kisslinger: investigation, formal analysis. R. Agrawal: writing – review & editing, validation, supervision, resources, methodology, funding acquisition.

Conflicts of interest

The authors declare no conflict of interest.

Data availability

The data supporting this article have been included in the SI. Supplementary information: Information on additional X-ray diffraction, TEM, HRTEM, HAADF-STEM, STEM-EDX and SEM-EDX. See DOI: **https://doi.org/10.1039/d5tc02508g**

Acknowledgements

The authors acknowledge the National Science Foundation's financial support through grant 2422591 (DMR). This research used Electron Microscopy facilities of the Center for Functional Nanomaterials (CFN), a U.S. Department of Energy Office of Science User Facility, at Brookhaven National Laboratory under contract no. DE-SC0012704

References

1 K. V. Sopiha, C. Comparotto, J. A. Márquez and J. J. S. Scragg, Chalcogenide Perovskites: Tantalizing Prospects, Challenging Materials, *Adv. Opt. Mater.*, 2022, **10**(3), 2101704, DOI: **10.1002/adom.202101704**.

2 Y. Han, X. Fang and Z. Shi, Advances in Chalcogenide Perovskites: Fundamentals and Applications, *Appl. Phys. Rev.*, 2024, **11**(2), 021338, DOI: **10.1063/5.0203535**.

3 S. Perera, H. Hui, C. Zhao, H. Xue, F. Sun, C. Deng, N. Gross, C. Milleville, X. Xu, D. F. Watson, B. Weinstein, Y. Y. Sun, S. Zhang and H. Zeng, Chalcogenide Perovskites - an Emerging Class of Ionic Semiconductors, *Nano Energy*, 2016, **22**, 129–135, DOI: **10.1016/j.nanoen.2016.02.020**.

4 S. Agarwal, K. C. Vincent and R. Agrawal, From Synthesis to Application: A Review of BaZrS3 Chalcogenide Perovskites, *Nanoscale*, 2025, **17**(8), 4250–4300, DOI: **10.1039/D4NR03880K**.

5 M. Surendran, S. Singh, H. Chen, C. Wu, A. Avishai, Y. Shao and J. Ravichandran, A Hybrid Pulsed Laser Deposition Approach to Grow Thin Films of Chalcogenides, *Adv. Mater.*, 2024, **36**(19), 2312620, DOI: **10.1002/adma.202312620**.

6 D. C. Hayes, S. Agarwal, K. C. Vincent, I. M. Aimiuwu, A. A. Pradhan, M. C. Uible, S. C. Bart and R. Agrawal, A Reliable, Colloidal Synthesis Method of the Orthorhombic Chalcogenide Perovskite, BaZrS3, and Related ABS3 Nanomaterials (A = Sr, Ba; B = Ti, Zr, Hf): A Step Forward for Earth-Abundant, Functional Materials, *Chem. Sci.*, 2025, **16**(3), 1308–1320, DOI: **10.1039/D4SC06116K**.

7 I. Sadeghi, K. Ye, M. Xu, Y. Li, J. M. LeBeau and R. Jaramillo, Making BaZrS3 Chalcogenide Perovskite Thin Films by Molecular Beam Epitaxy, *Adv. Funct. Mater.*, 2021, **31**(45), 2105563, DOI: **10.1002/adfm.202105563**.

8 M. Surendran, B. Zhao, G. Ren, S. Singh, A. Avishai, H. Chen, J.-K. Han, M. Kawasaki, R. Mishra and J. Ravichandran, Quasi-Epitaxial Growth of BaTiS3 Films, *J. Mater. Res.*, 2022, **37**(21), 3481–3490, DOI: **10.1557/s43578-022-00776-y**.

9 T. R. Paudel and E. Y. Tsymbal, Evaluating the Thermoelectric Properties of BaTiS3 by Density Functional Theory, *ACS Omega*, 2020, **5**(21), 12385–12390, DOI: **10.1021/acsomega.0c01139**.

10 H. Chen; S. Singh; H. Mei; G. Ren; B. Zhao; M. Surendran; Y.-T. Wang; R. Mishra; M. A. Kats and J. Ravichandran, *Molten Flux Growth of Single Crystals of Quasi-1D Hexagonal Chalcogenide $BaTiS_3$, 2024.*

11 F. Yang, K. Li, M. Fan, W. Yao, L. Fu, C. Xiong, S. Jiang, D. Li, M. Xu, C. Chen, G. Zhang and J. Tang, Strongly Anisotropic Quasi-1D BaTiS3 Chalcogenide Perovskite for Near-Infrared Polarized Photodetection, *Adv. Opt. Mater.*, 2023, **11**(5), 2201859, DOI: **10.1002/adom.202201859**.

12 N. Humphrey, A. Tsung, S. Singh, A. Irshad, B. Zhao, S. Narayan, J. Ravichandran and S. Mallikarjun Sharada, The Hydrogen Evolution Activity of BaZrS3, BaTiS3, and BaVS3 Chalcogenide Perovskites, *ChemPhysChem*, 2024, **25**(13), e202300953, DOI: **10.1002/cphc.202300953**.

13 D. Zilevu and S. E. Creutz, Shape-Controlled Synthesis of Colloidal Nanorods and Nanoparticles of Barium Titanium Sulfide, *Chem. Mater.*, 2021, **33**(13), 5137–5146, DOI: **10.1021/acs.chemmater.1c01193**.

14 S. Agarwal, K. C. Vincent, J. W. Turnley, D. C. Hayes, M. C. Uible, I. Durán, A. S. M. Canizales, S. Khandelwal, I. Panicker, Z. Andoh, R. M. Spilker, Q. Ma, L. Huang, S. Hwang, K. Kisslinger, S. Svatek, E. Antolin, S. C. Bart and R. Agrawal, Breaking Barriers in Chalcogenide Perovskite Synthesis: A Generalized Framework for Fabrication of BaMS3 (M = Ti, Zr, Hf) Materials, *Adv. Funct. Mater.*, 2024, **34**(46), 2405416, DOI: **10.1002/adfm.202405416**.

15 H. Hahn and U. Mutschke, Untersuchungen Über Ternäre Chalkogenide. XI. Versuche Zur Darstellung von Thioperowskiten, *Z. Anorg. Allg. Chem.*, 1957, **288**(5–6), 269–278, DOI: **10.1002/zaac.19572880505**.

16 J. H. A. AlShuhaib, *Exploring Novel Applications of Chalcogenide Perovskites*, Autonomous University of Madrid, Madrid, 2024.

17 J. Cuya, N. Sato, K. Yamamoto, H. Takahashi and A. Muramatsu, Thermogravimetric Study of the Sulfurization of SrTiO3 Nanoparticles Using CS2, *Thermochim. Acta*, 2004, **419**(1–2), 215–221, DOI: **10.1016/j.tca.2004.01.033**.

18 S. Perera, H. Hui, C. Zhao, H. Xue, F. Sun, C. Deng, N. Gross, C. Milleville, X. Xu, D. F. Watson, B. Weinstein, Y.-Y. Sun, S. Zhang and H. Zeng, Chalcogenide Perovskites – an Emerging Class of Ionic Semiconductors, *Nano Energy*, 2016, **22**, 129–135, DOI: **10.1016/j.nanoen.2016.02.020**.

19 J. H. A. Shuhaib, J. F. Fernández, J. Bodega, J. R. Ares, I. J. Ferrer and F. Leardini, Synthesis, Optical Band Gap and Thermoelectric Properties of Sr1 + xTiS3-y Chalcogenide Perovskites, *Mater. Res. Bull.*, 2023, **167**, 112405, DOI: **10.1016/j.materresbull.2023.112405**.

20 B. Okai, K. Takahashi, M. Saeki and J. Yoshimoto, Preparation and Crystal Structures of Some Complex Sulphides at High Pressures, *Mater. Res. Bull.*, 1988, **23**(11), 1575–1584, DOI: **10.1016/0025-5408(88)90245-0**.

21 Y. Han, J. Zhang, Z. Yu, J. Zhu, X. Xing, Q. Mo, L. Li, H. Gao, X. Chen, Z. Ma, J. Zhang, Y. Zhang, M. Li and Z. Shi, Integration of Photo- and Thermal-Detection Based on Hexagonal Chalcogenide Perovskite Sr8Ti7S21 with Full Spectrum Absorption, *Adv. Funct. Mater.*, 2025, **35**, 2500792, DOI: **10.1002/adfm.202500792**.

22 H. Mei, G. Ren, B. Zhao, J. Salman, G. Y. Jung, H. Chen, S. Singh, A. S. Thind, J. Cavin, J. A. Hachtel, M. Chi, S. Niu, G. Joe, C. Wan, N. Settineri, S. J. Teat, B. C. Chakoumakos, J. Ravichandran, R. Mishra and M. A. Kats, Colossal Optical Anisotropy from Atomic-Scale Modulations, *Adv. Mater.*, 2023, **35**(42), 2303588, DOI: **10.1002/adma.202303588**.

23 D. Yang, Y. Han, M. Li, C. Li, W. Bi, Q. Gong, J. Zhang, J. Zhang, Y. Zhou, H. Gao, J. Arbiol, Z. Shi, G. Zhou and A. Cabot, Highly Conductive Quasi-1D Hexagonal Chalcogenide Perovskite Sr8Ti7S21 with Efficient Polysulfide Regulation in Lithium-Sulfur Batteries, *Adv. Funct. Mater.*, 2024, **34**(42), 2401577, DOI: **10.1002/adfm.202401577**.

24 D. Zilevu and S. E. Creutz, Solution-Phase Synthesis of Group 3–5 Transition Metal Chalcogenide Inorganic Nanomaterials, *Chem. Commun.*, 2023, **59**(57), 8779–8798, DOI: **10.1039/D3CC01731A**.

25 S. Agarwal, J. W. Turnley, A. A. Pradhan and R. Agrawal, Moderate Temperature Sulfurization and Selenization of Highly Stable Metal Oxides: An Opportunity for Chalcogenide Perovskites, *J. Mater. Chem. C*, 2023, **11**(45), 15817–15823, DOI: **10.1039/D3TC02716C**.

26 D. Zilevu, O. O. Parks and S. E. Creutz, Solution-Phase Synthesis of the Chalcogenide Perovskite Barium Zirconium Sulfide as Colloidal Nanomaterials, *Chem. Commun.*, 2022, **58**(75), 10512–10515, DOI: **10.1039/D2CC03494H**.

27 R. Yang, A. D. Jess, C. Fai and C. J. Hages, Low-Temperature, Solution-Based Synthesis of Luminescent Chalcogenide Perovskite BaZrS3 Nanoparticles, *J. Am. Chem. Soc.*, 2022, **144**(35), 15928–15931, DOI: **10.1021/jacs.2c06168**.

28 M. Onoda, M. Saeki, A. Yamamoto and K. Kato, Structure Refinement of the Incommensurate Composite Crystal Sr1.145TiS3 through the Rietveld Analysis Process, *Acta Crystallogr., Sect. B:Struct. Sci.*, 1993, **49**(6), 929–936, DOI: **10.1107/S0108768193005324**.

29 S. Niu, H. Zhao, Y. Zhou, H. Huyan, B. Zhao, J. Wu, S. B. Cronin, H. Wang and J. Ravichandran, Mid-Wave and Long-Wave Infrared Linear Dichroism in a Hexagonal Perovskite Chalcogenide, *Chem. Mater.*, 2018, **30**(15), 4897–4901, DOI: **10.1021/acs.chemmater.8b02279**.

30 H. Karlsson, *Four-Dimensional Modeling of Two Ternary Columnar Composite Compounds*, Lund University, Sweden, 2015.

31 O. Gourdon, L. Cario, V. Petricek, J. M. Perez-Mato and M. Evain, Synthesis, Structure Determination, and Twinning of Two New Composite Compounds in the Hexagonal Perovskite-like Sulfide Family: Eu8/7TiS3 and Sr8/7TiS3, *Z. Kristallogr. – Cryst. Mater.*, 2001, **216**(10), 541–555, DOI: **10.1524/zkri.216.10.541.20366**.

32 M. Onoda, M. Saeki, A. Yamamoto and K. Kato, Structure Refinement of the Incommensurate Composite Crystal Sr1.145TiS3 through the Rietveld Analysis Process, *Acta Crystallogr., Sect. B:Struct. Sci.*, 1993, **49**(6), 929–936, DOI: **10.1107/S0108768193005324**.

33 A. A. Pradhan, M. C. Uible, S. Agarwal, J. W. Turnley, S. Khandelwal, J. M. Peterson, D. D. Blach, R. N. Swope, L. Huang, S. C. Bart and R. Agrawal, Synthesis of BaZrS3 and BaHfS3 Chalcogenide Perovskite Films Using Single-Phase Molecular Precursors at Moderate Temperatures, *Angew. Chem., Int. Ed.*, 2023, **62**, e202301049, DOI: **10.1002/anie.202301049**.

34 M. Ishii and M. Saeki, Raman and Infrared Spectra of BaTiS3 and BaNbS3, *Phys. Status Solidi B*, 1992, **170**(1), K49–K54, DOI: **10.1002/pssb.2221700149**.

35 C. J. Carmalt, E. S. Peters, I. P. Parkin and D. A. Tocher, Reactivity of Tetrakisdimethylamido-Titanium(Iv) and -Zirconium(Iv) with Thiols, *New J. Chem.*, 2005, **29**(4), 620, DOI: **10.1039/b413060j**.

36 S. Suresh and A. R. Uhl, Present Status of Solution-Processing Routes for Cu(In,Ga)(S,Se)2 Solar Cell Absorbers, *Adv. Energy Mater.*, 2021, **11**(14), 2003743, DOI: **10.1002/aenm.202003743**.

37 S. Niu, B. Zhao, K. Ye, E. Bianco, J. Zhou, M. E. McConney, C. Settens, R. Haiges, R. Jaramillo and J. Ravichandran, Crystal Growth and Structural Analysis of Perovskite Chalcogenide BaZrS3 and Ruddlesden–Popper Phase Ba3Zr2S7, *J. Mater. Res.*, 2019, **34**(22), 3819–3826, DOI: **10.1557/jmr.2019.348**.

38 P. N. Dasgupta, X. Meng, W. J. Elam and B. F. A. Martinson, Atomic Layer Deposition of Metal Sulfide Materials, *Acc. Chem. Res.*, 2015, **48**(2), 341–348, DOI: **10.1021/ar500360d**.

39 D. Hiller, F. Munnik, J. López-Vidrier, D. Solonenko, J. Reif, M. Knaut, O. Thimm and E. N. Grant, Comparison of three titanium-precursors for atomic-layer-deposited TiO2 for passivating contacts on silicon, *J. Vac. Sci. Technol., A*, 2024, **42**(3), 032406, DOI: **10.1116/6.0003309**.